PNAS

Hot liquid marbles

Pritam K. Roy[1], Yui Takai[1], Rui Matsubara[1], Mizuki Tenjimbayashi[2] and Timothée Mouterde[1*]

1. The University of Tokyo, Department of Mechanical Engineering, School of Engineering, Hongo 7-3-1, Bunkyo, 113-0033, Tokyo, Japan.
2. Research Center for Materials Nanoarchitectonics (MANA), National Institute for Materials Science (NIMS), 1-1 Namiki, Tsukuba, Ibaraki, 305-0044, Japan.

Timothée Mouterde

Email: mouterde@g.ecc.u-tokyo.ac.jp

Author Contributions: T.M. conceived the project. T.M. and P.K.R designed the project. M.T. provided particles and contributed to the discussions. P.K.R. performed most experiments to which Y.T. and R.M. also participated. P.K.R., T.M. and Y.T. performed the analyses. T.M. built the model. T.M. and P.K.R. wrote the manuscript with inputs from Y.T. and M.T.

Competing Interest Statement: T.M. and P.K.R declare that they are listed as an inventor on a patent application, Japanese Patent Application No. 2024-099815. that relates to the findings described in this manuscript.

Classification: Physical science, Applied Physical Sciences.

Keywords: drops; liquid marbles; static friction; condensation.

This PDF file includes:

Main Text (with Figures)
Figures 1 to 5

Abstract

In the insect realm, liquids become traps due to capillary and viscous forces dominant at their scale. Yet, aphids handle the highly viscous honeydew droplets they secrete, by coating them with hydrophobic wax powder which maintains an air layer between their body and the liquid. These coated droplets, known as liquid marbles, exhibit low friction and high mobility, enabling manipulation of small liquid volumes which is useful for biomedical analysis where sample volumes are limited, chemistry to reduce chemical waste, or digital microfluidics for large-scale cell culturing and drug testing. For such applications—including exothermic reactions or biological studies typically conducted above room temperature—the ability to carry hot liquid is important but remains unexplored. This article investigates the stability and static friction of hot liquid marbles placed on a substrate cooler by ΔT. We show that for large ΔT, the core liquid evaporates and condenses within the air layer below the marbles creating liquid bridges resulting in marble rupture on hydrophilic substrates and increased static friction on hydrophobic ones. The temperature difference modifies the static friction nature, solid friction dominates at small ΔT and is replaced by a liquid pinning force at larger ΔT due to the increased liquid bridge density resulting from condensation. Finally, our study provides ways to avoid the rupture and increased static friction of hot liquid marbles due to the bridge formation by increasing the particle size, decreasing the liquid volatility, or using nanostructured superhydrophobic substrates.

Significance Statement

Droplets coated with hydrophobic particles, known as liquid marbles, exhibit ultra-low friction as an air layer separates liquid from solid. This enables manipulation of small liquid volumes without losses, with applications in biomedical analysis, digital microfluidics, and chemistry. Yet, their capacity to carry hot liquids remains unexplored. This research examines the stability and static friction of hot liquid marbles placed on cooler substrates. We show that, on hydrophilic surfaces, temperature differences cause rupture due to condensation bridging the core liquid with the substrate, while on hydrophobic surfaces, bridging increases static friction, shifting its nature from solid to liquid. Our model provides strategies to prevent rupture and friction, with larger particles, lower liquid volatility, or superhydrophobic substrates, broadening liquid marbles' potential.

Introduction

Below the millimeter scale, droplets are generally pinned due to the dominance of viscous and capillary forces [1-4]. Limiting their pinning is essential for applications that require manipulating small amounts of liquids, such as chemistry—where reducing chemical waste is crucial—or in biomedical analysis and biology, where sample volumes are limited. Low static friction and high mobility can be achieved with superhydrophobic materials on which hydrophobic structures stabilize an air layer between the liquid and the solid, limiting the effect of surface tension and viscosity [5-6]. Another approach consists of forming liquid marbles by covering the drop with hydrophobic powder [7]. The hydrophobic structure is then directly embedded at the liquid surface, making the non-wetting state independent of the substrate. While liquid marbles are sometimes regarded as a simple variation of superhydrophobic surfaces; fixing the hydrophobic textures on a solid or leaving them mobile at a liquid surface leads to distinct wetting behavior compared to superhydrophobic surfaces. For example, drops on superhydrophobic materials and liquid marbles have different static and dynamic frictions [8-9] and bouncing properties [10-14]. The particles' shell also allows for bringing additional functions to liquid marbles by modifying the particles' properties, thus offering them a strong potential for applications [15-17]. Notably, magnetite particles allow the positioning and opening of liquid marbles with magnetic fields [18], while silver particles permit ultrasensitive electrochemistry and surface-enhanced Raman spectroscopy [19], suitable for lab-on-a-chip applications. The literature on liquid marbles continues to expand in domains as diverse as biology [20-22], chemistry [23], sensing [24-25] or materials science [26]. Among these applications, temperature plays an important role in enabling

various functionalities. For instance, thermal Marangoni flows allow to move marbles placed on liquid bath [27-30], while the on-demand release of the marble content can be achieved through the melting of wax particles upon heating [31]. When liquid marbles are placed on a hot surface, their particle shell can limit evaporation and prevent boiling similar to the Leidenfrost effect [32]. Conversely, upon freezing, the properties of the particle shell control the final shape of the liquid marbles, which can deviate from that of drops on superhydrophobic surfaces [33-34]. Additionally, cooling down liquid marbles provides a noninvasive refilling mechanism through the condensation of atmospheric water across the porous shell [35]. Condensation effects may also occur in the opposite scenario, when the core liquid is warmer than its surroundings. This raises the broader question of marbles' ability to contain and transport hot liquids, an aspect that remains largely unexplored. In this study, we investigate the stability and static friction of hot liquid marbles placed on a cooler substrate. This situation is particularly relevant for biology and chemistry, where cell cultures, analyses at 37°C or exothermic reactions can create temperature differences between the liquid and the substrate.

Hot liquid marble stability

We first investigate the stability of hot liquid marbles in contact with hydrophobic or hydrophilic silicon wafers kept at room temperature T_o = 24 ± 1°C. Hydrophobicity is obtained by chemical vapor deposition of 1H,1H,2H,2H-perfluorodecyltrichlorosilane (see Methods section 'Substrate preparation'), which provides water advancing and receding contact angles of θ_a = 126 ± 2°, θ_r = 99 ± 2°, respectively. This surface is compared with hydrophilic pristine silicon, θ_a = 23 ± 2°; θ_r = 12 ± 2° (see SI Appendix, Text S1 and Fig. 1). We form the hot liquid marbles by coating water drops with temperature $T_o + \Delta T$, density ρ, and volume Ω = 50 µL with lycopodium grains of typical size $d \approx 30$ µm (Fig. 1a), so that there is an initial temperature difference ΔT between the marble and its substrate (see Methods section 'Hot liquid marbles preparation' and SI Appendix, Fig. S2). We observe the evolution of the hot liquid marble and show its state on Fig. 1b around 3 minutes after deposition for ΔT = 0°C and ΔT = 16°C, respectively. Without temperature difference (ΔT = 0°C, left), the liquid marble shape and apparent contact angle are independent of the substrate wettability, as expected due to the absence of contact between the liquid and the substrate. Conversely, when the water is warmer than the substrate (ΔT = 16°C, right) the liquid marble shape strongly depends on the surface wettability. In the hydrophilic case, the liquid marble ruptures and spreads on the substrate, resulting in a decreased apparent contact angle ~ 34 ± 2° and an increased contact radius ~ 12 mm. In contrast, the temperature difference in the hydrophobic case only results in a minimal change of shape and apparent contact angle when compared with the isothermal situation, ΔT = 0°C. We quantify the shape evolution by measuring the final apparent contact angle θ_f of the hot liquid marble as a function of ΔT (Fig. 1c). On the hydrophobic substrate (red data), θ_f slightly decreases from 157 ± 2° to 144 ± 2° when increasing ΔT from 0 to 29°C. In contrast, with the hydrophilic substrate (blue data), when the temperature exceeds a critical value $\Delta T_c \approx 1.5 \pm 1$°C, θ_f drops from a plateau at 154 ± 2° to a lower plateau at 18° ± 2°. The values of the two plateaus correspond to the isothermal liquid marble apparent contact angle for ($\Delta T < \Delta T_c$) and to the water contact angle on the pristine silicon wafer ($\Delta T > \Delta T_c$) (SI Appendix, Fig. S1).

To understand the rupture above ΔT_c, using a high-speed camera (Fastcam Nova S6, Photron), we record the evolution of the apparent contact angle θ with time t (taking t = 0 when the marble first touches the substrate) for different initial ΔT and we report the measurements in Figure 1d (Movie S1). The graph reveals two types of curves: for $\Delta T < \Delta T_c$, the marble is stable, and the contact angle remains constant at 154 ± 2° as expected from the results of Figure 1c. For $\Delta T > \Delta T_c$, the liquid marble is initially stable with an apparent contact angle value close to the isothermal case (ΔT = 0°C) but ruptures after a time t_r (Fig. 1d, vertical dashed lines) when its apparent contact angle drops within a few tens of milliseconds to the small final value shown in the Figures 1b and 1c. This graph also reveals that the rupture time t_r decreases with increasing temperature differences, which we now further explore. We plot in Figure 1e the rupture time t_r as a function of ΔT, the graph contains two main information: (i) t_r is a decreasing function of ΔT, (ii)

slightly above ΔT_c, the rupture time is very sensitive to the temperature difference as increasing ΔT from 3 to 14°C results in a ~170-fold decrease of t_r from ~ 6 s to ~ 36 ms.

Origin of the hot liquid marbles' rupture

The hot liquid marble stability depends on the substrate wettability which implies that the core water contacts with the substrate. To unveil this mechanism, we place the liquid marble on a hydrophilic glass substrate (see Methods section 'Substrate preparation' and SI Appendix, Fig. S1) and observe the bottom air layer with a total internal reflection (TIR) microscope (see Fig. 2a). The TIR microscope consists of illuminating the interface with a collimated light beam with an angle of incidence between the critical angle for glass/air and glass/water interfaces so that light is only transmitted at the glass/water interface (see Methods section 'Total Internal Reflection Microscope'). The images reflected at the interface between the bottom of the liquid marble and the glass slide are captured with a high-speed camera (Fastcam Nova S6, Photron) at a frame rate of 500 or 4000 fps for ΔT = 1.6°C and 16°C, respectively. The TIR movies reveal the dynamic of the water/substrate contacts. In the isothermal case (ΔT = 0°C), all the light is reflected to the camera (Fig. 2b). This demonstrates the absence of water/substrate contact due to the air layer formed by the particles and explains why, for ΔT = 0°C the liquid marble shape is independent of the substrate wettability (Fig. 1b, 1c). On the contrary, for hot liquid marbles ($\Delta T > 0$), shortly after deposition the contact area darkens due to the nucleation of condensation droplets below the marble which water/glass interface transmits light (Fig. 2c). For $\Delta T < \Delta T_c$ when the marbles are stable, the condensation evaporates after a few seconds to reach a final state where all the dark spots disappear, identical to that of isothermal liquid marbles (Fig. 2c top, Movie S2). For larger $\Delta T \approx$ 16°C (Fig. 2c bottom, Movie S2), condensation forms and grows quickly until $t \approx$ 0.46 s, when a darker spot appears and rapidly expands on the substrate. This corresponds to the marble rupture with the spreading of the core liquid on the hydrophilic substrate.

These observations allow us to explain and model the origin of the rupture mechanism: when the hot liquid marble is brought in contact with the colder substrate, the water vapor contained in the hot air surrounding the marble nucleates and condenses within the air layer separating the hot core liquid from the substrate. The difference of saturated vapor mass concentration $\Delta c_{sat}(\Delta T) = c_{sat}(T_o + \Delta T) - c_{sat}(T_o)$ between the hot evaporating interface at temperature $T_o + \Delta T$ and the colder condensation droplet kept at T_o, creates a diffusive vapor flux $D\Delta c_{sat}/h$ responsible for the condensate growth, where $D \approx 20$ mm^2 s^{-1} is the diffusion coefficient of water vapor in air, and h the distance between the core liquid and the condensation droplet (Fig. 2d). After a typical time $t_{cond} \sim \rho h^2/D\Delta c_{sat}(\Delta T)$, the condensation height reaches h and forms a liquid bridge between the core liquid and the substrate resulting in the liquid marble rupture. The TIR images reveal that the first bridging event (Fig. 2c, $t \approx$ 0.46 s) corresponds to the core liquid spreading on the hydrophilic substrate. Consequently, the relevant length h for rupture should be the minimum of the air layer thickness (Fig. 2d) which is on the order of the particle diameter $h \sim d$, hence the rupture time:

$$t_r \sim \rho d^2/D\Delta c_{sat}(\Delta T) \quad (1)$$

Taking the values previously mentioned for D and ρ, and using the Rankine formula for $c_{sat}(T)$ (see Methods section 'Saturated vapor concentration'), d is the only free parameter in Eq. (1), which we use as an adjustment parameter. The best fit is obtained for d = 19.7 ± 2.1 µm (95% interval of confidence) and plotted in black in Figure 1e. We find that our model captures well the evolution of the marble rupture time, and the value for d is in excellent agreement with the typical lycopodium diameter of ~ 30 µm (Fig. 1a and SI Appendix, Fig. S3a). However, this model predicts that even for small ΔT marbles should rupture while experiments show that they remain stable.

To understand the stability of marbles for $\Delta T < \Delta T_c$, we need to consider the liquid marble cooling due to the surrounding atmosphere. The condensation process only occurs while there is a

temperature difference between the liquid and the substrate, and the liquid marble remains stable if the condensation time t_r is larger than the cooling time τ which we now evaluate. Considering that the marble cools down due to heat transfer with the outside, the energy conservation of the marble writes $\rho C \Omega d\Delta T/dt = -\alpha S \Delta T$, where C is the specific heat capacity of water, α the water/air heat transfer coefficient and S is the liquid marble surface area. The temperature difference decays exponentially $\Delta T(t) = \Delta T_o \exp(-t/\tau)$ with a characteristic cooling time $\tau = (\Omega/S)^*\rho C/\alpha$. In the range of volume explored, liquid marbles are flattened by gravity and can be approximated as cylinders of base contact radius R_c and height $2a$, where $a = (\gamma/\rho g)^{1/2}$ is the capillary length, with γ the effective marble surface tension [36] which we approximate as that of pure water at room temperature $\gamma \approx 72$ mN/m and $g \approx 9.81$ m/s^2 the acceleration of gravity. With this approximation, the volume-to-surface ratio takes a simple expression: $\Omega/S \sim 2\pi R_c^2 a/2\pi R_c^2 \sim a$, hence the cooling time $\tau \sim \rho C a/\alpha$. Taking $\alpha \approx 1000$ W/m^2, $\rho \approx 1000$ kg/m^3 and $C \approx 4100$ J/kg/K, we find τ to be around 10 s. This value is in excellent agreement with the time evolution of ΔT measured by inserting a thermocouple in liquid marbles for different initial ΔT and plotted in Figure 2e, where all the data are well fitted by an exponential decay with cooling time of $\tau = 11$ s (plain line).

The cooling dynamics allow us to predict the transition from stable to rupturing marble, which should occur for the temperature difference ΔT_c where the condensation time equals the cooling time $t_r(\Delta T_c) = \tau$. For $\Delta T < \Delta T_c$, ($t_r > \tau$) the marble cools faster than the condensation time required to form the first liquid bridge which explains the marble stability as the core liquid remains disconnected from the substrate. Conversely, for $\Delta T > \Delta T_c$ condensation is faster and a liquid bridge forms before thermalization, resulting in the marble rupture. For small ΔT, we approximate $\Delta c_{sat}(\Delta T)$ with a Taylor expansion of the Rankine formula: $\Delta c_{sat}(\Delta T) = c_{sat}(T_o) 5120 \Delta T/T_o^2$, this leads to a simplified expression of Eq. (1) $t_r = \rho d^2 T_o^2/5120 D c_{sat}(T_o) \Delta T$, which we plot on Fig. 1e in red and is found to also nicely fits the data with $d \approx 18.3 \pm 2.6$ µm. This approximation also provides an explicit formula for ΔT_c: $\Delta T_c = \rho d^2 T_o^2/5120 D c_{sat}(T_o) \tau$. Using the previously defined values, our model predicts $\Delta T_c = 1.2$ °C, which indeed separates the stable from unstable marbles (Fig. 1c, 1e).

Hot liquid marbles static friction

The air layer between the substrate and the liquid is responsible for both the large apparent contact angle and the low friction of the liquid marbles. The invasion of the air layer by condensation results, on hydrophilic substrates, in the marble rupture characterized by a low apparent contact angle and high static friction. Conversely, on hydrophobic substrates, the hot liquid marble shape is only marginally affected by the temperature difference (Fig. 1c), here we explore how condensation affects the static friction of hot liquid marbles.

We deposit lycopodium hot marbles ($\Omega = 50$ µL) on a hydrophobic silicon substrate, we wait for a minute—a time larger than the cooling time τ—to avoid transient effects (see SI Appendix, Text S2 and Fig. S4) and we then increase the tilt angle between the surface and horizontal (see Methods section 'Static friction experiments') until we reach the critical value α^* where the marble departs from the substrate (Fig. 3a, left images and Movie S3). This slope provides us with the static friction F which is equal to the projected weight $mg \sin \alpha^*$, where $m = \rho\Omega + m_p$ is the liquid marble mass with $\rho\Omega$ and m_p the liquid and particles mass, respectively (SI Appendix, Tables S1 and 2). We repeat this experiment for different ΔT and we plot in red in the Figure 3b, the static friction F as a function of ΔT. For temperature differences smaller than ~ 5°C, the friction remains constant around 13.5 ± 1.5 µN which corresponds to only 3% of the marble weight, thus marbles depart from their substrate for a small tilt angle 1.6 ± 0.5°. When increasing ΔT from 5 to 15°C the static friction rises by 25-fold before reaching a plateau at ~ 330 µN (~70% of the marble weight). The hot marbles are then strongly pinned and move only for large tilts around 45° (Fig. 3a left, Movie S3). To understand the static friction mechanism, we perform a separate experiment where we observe the wet contact, with the TIR setup previously described, ~ 5 minutes after deposition on a hydrophobic glass substrate (see Methods section 'Substrate preparation'). We show the

TIR images corresponding to each ΔT of Figure 3a (right images for each ΔT and SI Appendix, Fig. S5 and Movie S4). The images reveal two points: (i) contrary to the hydrophilic case, when condensation forms a bridge between the substrate and the core liquid, the marble does not spread on the substrate and the air layer below the marble is only partially invaded by water. We quantify this partial invasion of the air layer by defining the wetted fraction ϕ as the liquid/solid contact area normalized by the liquid marble contact area πR_c^2 where the contact radius R_c is measured from side view images (SI Appendix, Fig. S6). (ii) The wetted fraction ϕ, increases with the temperature difference ΔT from no contact $\phi = 0$ (ΔT = 3°C) to a very wet contact $\phi \approx 0.9$ at ΔT = 29°C.

We plot in Figure 3b (blue data, right-side vertical scale), the wetted fraction ϕ as a function of ΔT, the evolution of $\phi(\Delta T)$ is very similar to the friction $F(\Delta T)$ with a low plateau value below 5°C, followed by a rapid increase up to 15°C from which ϕ plateaus. To confirm this observation, the temperature-induced static friction $\Delta F = F(\Delta T) - F(\Delta T = 0)$ is plotted as a function of ϕ, Figure 3c, this reveals the linearity between the two quantities $\Delta F \sim \phi$.

We further explore the nature of the static friction of hot liquid marbles by changing their size; for a given ΔT, we measure the evolution of the friction as a function of the marble volume Ω. The results, plotted in Fig. 3d with a log-log scale, reveal a change in the friction nature between low and high-temperature differences. At small ΔT (blue data), the static friction is small and seems linear with the volume $F \sim \Omega$, while for larger ΔT (red data), the friction is typically 20 times larger and the slope close to 0.5, $F \sim \Omega^{0.5}$.

Model of hot liquid marbles static friction

We now model the static friction of hot liquid marbles. At small ΔT, the data suggest a solid/solid friction as described by Jin *et al.* [8], the contact between the liquid marble and the substrate remains dry ($\phi = 0$), and the Coulomb friction applies. The static friction is proportional to the force normal to the substrate through a static friction coefficient μ: $F = \mu\, \rho\Omega g \cos\alpha$ which balanced with the horizontal component of the weight leads gives the critical tilting angle $\alpha^* = \text{atan}\,\mu$. At the sliding angle, neglecting the mass of the particles ($m_p/\rho\Omega \approx 0.02 << 1$, see Methods section 'Particles' weight measurements' and SI Appendix, Tables S1 and S2) the static friction can be rewritten as:

$$F_{dry} = \rho\Omega g \frac{\mu}{\sqrt{1+\mu^2}} \quad (2)$$

The equation (2) is plotted in blue in Figure 3d with $\mu = 0.023$ obtained from the sliding angle for ΔT = 0°C. It describes well the static friction of marbles in the low-temperature regime and explains the linear dependency with the volume, *i.e.* $F \sim \Omega$.

We then model the case where ΔT is sufficiently large for condensation to partially fill the air layer ($\phi > 0$). The liquid bridges create an additional force: moving the receding contact line by dx requires replacing the liquid/solid interface of area $\phi\pi R_c dx$ with an air/solid and a liquid/air interface. The required energy corresponds to the static friction force work and writes $F dx = \phi\pi R_c dx\gamma(1 + \cos\theta_o)$ with θ_o the Young contact angle of the liquid on the subjacent substrate. As previously mentioned, for the studied volumes, liquid marbles are flattened by gravity so that their volume Ω is that of a cylinder of base πR_c^2 and height $2a$. Thus, the contact radius writes $R_c \approx (\Omega/2a\pi)^{1/2}$ and we obtain the static friction force:

$$F_{wet} \approx \phi\gamma(1 + \cos\theta_o)(\pi\Omega/2a)^{1/2} \quad (3)$$

Qualitatively, our model predicts that static friction should be proportional to the wetted surface area $F \sim \phi$, which is consistent with the force and TIR measurements shown in Figures 3b and 3c. Furthermore, the model also captures the increase of the friction with the square root of the

volume $F \sim \Omega^{1/2}$ observed for large ΔT in Fig. 3d. Quantitatively, taking Ω = 50 µL, γ = 72 mN/m, a = 2.7 mm, and the measured value of θ_o = 99°, Equation 3 is best fitted to the experimental data in Fig. 3c with a prefactor 1.19 ± 0.12 (95% confidence level) as represented on Fig. 3c by the red curve and the blue shaded area. Using the same prefactor, we plot our model Eq. (3) in Figure 3d, taking for the wetted area $\phi \approx 0.9$ measured at large ΔT (Fig. 3b). We also find an excellent agreement with the experimental data and the value of the adjustment coefficient very close to unity confirming that our model describes quantitatively the static friction of hot marbles. The small deviation observed may stem from the approximation of the contact radius, $R_c \approx (\Omega/2a\pi)^{1/2}$, which remains accurate within 10% over the explored volume range or from the small relative variation (13% on average), of R_c with ΔT, which we did not account for (Fig. S6). Alternatively, it could arise from the contact angle uncertainty ε, which introduces a relative force uncertainty: $|F_{wet}(\theta_o + \varepsilon) - F_{wet}(\theta_o)|/|F_{wet}(\theta_o)| = |\varepsilon \sin \theta_o|/(1 + \cos \theta_o)$. For θ_o = 99° and $\varepsilon = 2°$, this results in an error of only 4%, though it increases for superhydrophobic substrates where θ_o approaches 180°.

These results clarify the friction transition, as the temperature difference ΔT increases, the formation of liquid bridges transforms the nature of the static friction from the low dry friction F_{dry} [Eq. (2)] characteristic of liquid marbles, to a significantly larger wet pinning force F_{wet} [Eq. (3)]. For 50 µL marbles, the crossover occurs when the wetted area ϕ is as small as 4% which further demonstrates why avoiding liquid/solid contact is key to the low friction of non-wetting states in general. This value of the liquid/solid contact fraction is typically that of superhydrophobic materials which explains the similar pinning strength despite their difference of nature.

Dry to wet static friction transition temperature – effect of particle size and liquid volatility

Our model predicts the amplitude of the static friction of hot liquid marbles depending on the evolution of the fraction of wetted area ϕ, we now focus on understanding the critical temperature at which ϕ (hence F) increases leading to the dry-to-wet friction transition. The transition depends on the dynamics of the liquid bridge formation, a mechanism similar to the one discussed for the hot liquid marble stability on hydrophilic substrates where both the thickness of the air layer and the liquid volatility controlled by Δc_{sat} play a crucial role. We first investigate the effect of the average air layer thickness H on the static friction. In addition to the lycopodium previously used ($d \approx 30$ µm), we test two other kinds of particles with different sizes: fumed silica nanoparticles ($d \approx 40$ nm), and hydrophobic glass beads ($d \approx 100$ µm) (SI Appendix, Fig. S3 and Methods section 'Hydrophobic glass beads preparation'). While the minimum thickness of the air layer h is determined by the particle size d, the average thickness H may differ from it due to particle aggregation (Fig. 2d). To measure H, we dye the marble water core and a glass substrate with Rhodamine B (see Methods section 'Air layer thickness measurement'), a fluorescent amphiphilic molecule, and we take 3D images of the bottom of the liquid marbles (Fig. 4a) with a confocal microscope (SP8, Leica). Rhodamine B at the substrate/air and liquid/air interfaces allows us to visualize the air layer and to measure its thickness H, and we obtain 30 ± 3 µm; 56 ± 2 µm and 242 ± 8 µm, for fumed silica nanoparticles, lycopodium and glass beads, respectively (SI Appendix, Fig. S7).

We plot in Figure 4b, the static friction force as a function of ΔT for the fumed silica nanoparticles (blue triangles) and glass beads (green squares) that we compare with the previous data for lycopodium (red disks). The static friction for smaller air layer thickness ($H \approx 30 \pm 3$ µm, blue triangles), has three notable features: (i) the shape of the curve is similar to that of lycopodium: the static friction is constant at low ΔT (dry friction) before rapidly increasing to reach a plateau (wet pinning). (ii) The transition temperature between the two regimes is around $\Delta T \approx 5$°C a value smaller than that of lycopodium ($\Delta T \approx 12$°C). (iii) The plateau value of the static friction at large ΔT is identical to that measured for lycopodium, which confirms that the particles' size does not change the maximum friction as predicted by our model. In contrast, the static friction curve for thicker air layer notably differs (glass beads, $H \approx 242 \pm 8$ µm, green squares); the increase between low and high temperature is much smaller, only twofold, compared to the 25-fold

increase observed with lycopodium and silica particles. We note that for all particles, the static friction varies with the wetted fraction measured with the TIR microscope (SI Appendix, Fig. S5 and S8 and Movies S5 and S6). For ΔT = 29°C higher frictions for lycopodium and silica nanoparticles correspond to larger wetted area (Fig. 4c, blue and red frames), while the quasi absence of wet contact coincides with the low friction for glass beads (Fig. 4c, green frame).

We now test the effect of the liquid volatility which should also affect the liquid bridge formation. To this end, we measure the static friction of lycopodium hot liquid marbles made with glycerol, a liquid with low volatility (vapor pressure about 10,000 times lower than that of water) due to its strong hydrogen bond network [37]. The static friction of hot glycerol marbles is plotted in Figure 4d as a function of ΔT (black diamonds), the difference with water marbles (red disks) is striking: the friction of glycerol marbles always remains in the dry friction regime below 10 µN for the whole range of explored temperature. This observation is confirmed by the absence of liquid/solid contacts observed with TIR microscopy even for large ΔT = 29°C (Fig. 4c, black frame and SI Appendix, Fig. S9).

We now model the occurrence of the dry-to-wet static friction transition. The transition happens due to the liquid bridge formation, governed by the cooling and condensation dynamics. The liquid cools down with a characteristic time $\tau \sim \rho Ca/\alpha$ during which the temperature difference maintains a water vapor flux $D\Delta c_{sat}(\Delta T)/H$ causes condensation to grow within the air layer to a typical maximum height $\delta \sim \tau D\Delta c_{sat}(\Delta T)/\rho H$. We note here that confocal images revealed that the interface is not covered by a monolayer of particles, which makes the air layer thickness non-uniform. On hydrophilic substrates, the minimum of the air layer thickness, on the order of the particle size *d*, will be the rupture point as a single liquid bridge will let the core liquid spread on the surface. Conversely, on hydrophobic substrates, a single liquid bridge only marginally affects the static friction. The bridge forming between hydrophobic particles as a typical size on the order of the particle diameter *d* which increases the wetted area ϕ by a quantity on the order of $\sim d^2/R_c^2$, this gives with Eq. (3) and for a 50 µL lycopodium marbles, an increase of the friction force around $\sim$ 0.3 µN, a value much smaller than the dry friction $\sim$ 13.5 ± 2 µN. Thus, the static friction increases significantly only when the condensation height δ reaches the average distance between the substrate and the liquid interface given by *H* that we previously measured (Fig. 4a). Hence, we expect the static friction to jump at ΔT_c when the ratio between the average air layer thickness and the maximum condensation height given by:

$$H/\delta = \rho H^2/D\Delta c_{sat}(\Delta T_c)\tau \quad (4)$$

becomes of order 1. To test our model, for each data point of Figures 4b and 4d, we plot in Figure 4e, the value of H/δ predicted by Equation (4) as a function of ΔT and we classify the data into two categories by comparing the increase of static friction from the dry state: $\Delta F = F - F(\Delta T = 0)$, with the maximum force $F_{max} = F_{wet}(\phi = 1)$, which is around 330 µN. The low static friction points, defined as $\Delta F < F_{max}/2$, are marked in green, while the high static friction points, $\Delta F > F_{max}/2$, are marked in red, where $F_{max} = F_{wet}(\phi = 1) \approx$ 330 µN. For glycerol data, we approximate the saturated vapor mass concentration with a modified Clarke and Glew equation [38], the diffusion coefficient by the Chapman-Enskog kinetic theory [39], (see Methods section 'Glycerol vapor diffusion coefficient') and the cooling time is estimated from direct measurements (SI Appendix, Fig. S10). We find that the low (green) and high (red) static friction states are separated by a line $H/\delta \approx 0.35$; a value close to $H/\delta \approx 1$ for which our model predicts the transition between dry and wet friction to occur.

Static friction prevention

Our findings give two practical ways to prevent the static friction of hot liquid marbles by avoiding the liquid bridge formation: (1) with low volatility liquids or (2) by increasing the thickness of the air layer with larger particles. These friction prevention methods limit the range of liquids and particles available for practical applications, but our model, Eq. (3), suggests a third way to limit

the hot marble static friction by increasing the substrate hydrophobicity. Indeed the friction proportional to (1 + cos θ_o) should vanish on superhydrophobic substrates where the contact angle tends to $180°$. We test this hypothesis with superhydrophobic samples made by coating a silicon wafer with a solution of hydrophobic silica nanoparticles (Glaco Mirror Coat Zero, Soft 99, Japan) which forms a nanoscale roughness on the surface (see Methods section 'Substrate preparation' and SI Appendix, Fig. S1). The nanoscale roughness is selected on purpose as it maintains its superhydrophobicity even with hot water [40]. The advancing and receding contact angles for water on this surface are $\theta_a \approx 161 \pm 2°$ and $\theta_r \approx 152 \pm 2°$, respectively (see SI Appendix, Fig. S1). We compare in Fig. 5a, $F(\Delta T)$ for lycopodium liquid marbles on the superhydrophobic (green triangles) and hydrophobic (red disks) substrates. On the superhydrophobic surface, the static friction is strongly reduced and remains always below 70 µN even for high-temperature differences, a value ~5 times smaller than that of the hydrophobic substrate. This decreased friction is in qualitative agreement with our model that predicts the force to be proportional to (1 + cos θ_o) a quantity that decreases when increasing the water contact angle on the substrate. To further test our model, we subtract from the total static friction the dry component $F(\Delta T = 0)$ which does not depend on the contact angle, and we plot in Fig. 5b the temperature-induced static friction $\Delta F = F - F(\Delta T = 0)$ normalized by (1+cos θ_o) as a function of ΔT. We take for θ_o the receding contact angle measured on the hydrophobic $\theta_H = 99°$ and superhydrophobic substrates $\theta_{SH} = 152°$. We find that (i) the increase of friction for hydrophobic ΔF_H and superhydrophobic ΔF_{SH} surfaces are close once normalized by (1+cos θ_o), and that using the superhydrophobic substrate reduces the static friction by $\Delta F_H/\Delta F_{SH} \approx (1 + \cos \theta_H)/(1 + \cos \theta_{SH})$ which is around 7. (ii) For both the hydrophobic and superhydrophobic cases the friction transition occurs around $\Delta T \approx 12°C$, which our model also explains as the transition depends only on the air layer thickness and the liquid volatility which are unchanged for these two cases (lycopodium with water). (iii) Finally, we note that while our model predicts a saturation for the superhydrophobic case, the static friction still increases with ΔT. This observation could deserve a separate study but should be related to condensation invading the nanostructures of the superhydrophobic coating leading to a partial Wenzel state which decreases θ_{SH} and increases the hot liquid affinity with the substrate [40].

Conclusion

In this study, we investigated the possibility to manipulate hot droplets using liquid marbles. Our results demonstrated that when placed on cooler substrates, hot liquid marbles exhibit distinct behaviors depending on the substrate wettability: they rupture on hydrophilic ones, while adhering to hydrophobic ones. This transition is due to condensation filling the air gap between the liquid and the substrate previously responsible for the low static friction and high mobility of the marbles. Remarkably, this condensation-induced transition not only increases the marble static friction, but it shifts its nature from solid (at thermal equilibrium) to liquid for hot marbles. These temperature-controlled rupture and static friction have potential for application in open millifluidics systems for bioanalysis or chemistry. Indeed, by creating a temperature difference between the marble and the substrate (for example by cooling the substrate with a Peltier or by heating up the liquid with a light source), one can selectively secure a marble position or disperse its content onto surface sensors for analysis.

Our model also provides ways to avoid hot liquid static adhesion, this can be achieved by tuning the liquid marble properties to delay the condensation-bridging with larger particles or lower liquid volatility, or by using nanostructured superhydrophobic substrates to limit the bridges' adhesion. While our study focused on marbles hotter than their substrate, it would be worth investigating the case of liquid marbles deposited on hot substrates and the practical case of rolling or impacting hot liquid marbles where in addition to the cooling and condensation time, the dynamic contact time should play a role.

Materials and Methods

Substrate preparation. The hydrophilic substrates are pristine silicon wafers (As ONE Corp., Japan) or glass slides. Using the same materials, we make the substrate hydrophobic by a 40 s activation step inside a plasma cleaner (Harrick Plasma, PDC-32G) followed by chemical vapor deposition of 1H,1H,2H,2H-perfluorodecyltrichlorosilane (Fluorochem Ltd.) in a reduced pressure atmosphere for 40 minutes. The superhydrophobic substrates are prepared by spraying a commercial solution of hydrophobic silica nanobeads dissolved in isopropyl alcohol (Glaco Mirror Coat Zero, Soft99). The substrates are then dried vertically and once the solvent evaporated, heated on a hot plate at 200°C for 30 minutes, we repeat this process three times. The substrates are renewed regularly to ensure their quality.

Hot liquid marbles preparation. To form hot liquid marbles, we heat up liquids (pure water or glycerol) and particles (lycopodium - Sigma Aldrich, fumed silica nanoparticles - Aerosil RY50, or glass beads - ASGB-320, As ONE Corp.) with a hot plate (SI Appendix, Fig. S2a). Using a micropipette, we deposit a droplet of hot liquid of volume Ω on the particles bed, the droplet is rolled until fully covered with particles and transferred on the substrate using a spatula made superhydrophobic with a Glaco coating. We measure the initial marble temperature ΔT as a function of the liquid bath temperature T_b by inserting a thermocouple inside the marbles. ΔT varies linearly with the plate temperature, and we use the best linear fit to estimate the temperature difference in the experiments: $\Delta T = 0.44(T_b - 23.9)$ with T_b in Celsius. The same method is used for glycerol and gives $\Delta T = 0.45(T_b - 23.9)$ (SI Appendix, Fig. S2b).

Total Internal Reflection Microscope. The TIR microscope consists of a collimated monochromatic LED light (M660L4, Thorlabs) shined on a dove prism (PS994, Thorlabs) with an angle of incidence β, adjusted to be larger than the total reflection angle for the glass/air interface $\beta_{air} = \text{asin}(n_{air}/n_g) \approx 41°$ but smaller than the total reflection angle for the glass/water $\beta_w = \text{asin}(n_w/n_g) \approx 62°$ or glass/glycerol interfaces $\beta_{gly} = \text{asin}(n_{gly}/n_g) \approx 77°$ with $n_{air} = 1.00$, $n_g = 1.51$, $n_w = 1.33$, $n_{gly} = 1.47$, the refractive index of air, glass, water and glycerol, respectively. The glass substrates are placed on top of the prism where a thin layer of immersion oil (Olympus IMMOIL-F30CC) is used to avoid light reflection at the prism/glass interface. The reflected light is captured with a high-speed camera (Fastcam Nova S6, Photron) and the movie's width deformed in the optical path is stretched back to the correct physical with a Matlab code.

Saturated vapor concentration. The water and glycerol saturated vapor concentration c_{sat} at a temperature T are derived from Dalton's law: $c_{sat}(T) = \rho_{air}(M_{liq}/M_{air})(P_{sat}(T)/P_o)$ with ρ_{air} the air density, M_{liq} and M_{air} the molar masses of water (resp. glycerol) and air, respectively, $P_{sat}(T)$ the saturated vapor pressure of water (resp. glycerol) at temperature T, and P_o is the atmospheric pressure. The saturated vapor pressure of water is estimated with the Rankine formula: $P_{sat}(T) = P_o \exp(13.7 - 5120/T)$, while that of glycerol is given by a modified Clarke and Glew equation proposed by Verevkin *et al.* [38]: $P_{sat}(T) = P_o \exp[(-23263/388.7 + 82273(1/388.7 - 1/T) - 83(388.7/T - 1 + \log(T/388.7)))/R]$, with R the molar gas constant.

Static friction experiments. The substrates are placed on a brass plate which stands on two lab jacks, the substrate is tilted by manually changing the height of one of the lab jacks. The angle is measured with a digital goniometer accurate to 0.1° (Monotaro, Japan). Images and movies are recorded with a Nikon D3200. Each point is obtained by averaging the static friction of five liquid marbles.

Particles' weight measurements. To estimate the particles' mass at the liquid interface, using a precision balance (Shinko Denshi Co., LTD., Model XFR–225W, accuracy of 0.01 mg), we measure the average weight m of 10 liquid marbles of volume Ω to which we subtract the average weight $\rho\Omega$ of ten water droplets of same volume. The volume is controlled with a

473 micropipette (M200, Monotaro). The particle mass is calculated by subtracting the droplet to the
474 marble weights $m_p = m - \rho\Omega$. The weights and particle to total mass ratio are summarized in SI
475 Appendix, Tables S1 and S2.

476 **Hydrophobic glass beads preparation.** The glass beads (ASGB-320, As ONE Corp.) are
477 rendered hydrophobic through chemical vapor deposition of Trichloro(1H,1H,2H,2H-tridecafluoro-
478 n-octyl)silane (Tokyo Chemical Industry Co., Ltd.,) on its surface. The glass bead surface is first
479 cleaned using plasma cleaner (PIB-10, Vacuum Device Inc.). Then, 5g of glass beads are sealed
480 in a glass container (diameter 90 mm and height 20 mm) with 30 µL of the silane and heated at
481 80°C for 12 hours.

482 **Air layer thickness measurement.** The air layer thickness between the marble and the
483 substrate is measured using a confocal microscope (Leica, SP8). To obtain the position of the
484 substrate and the marble, they are marked with Rhodamine B (Sigma-Aldrich), a fluorescent
485 molecule with a peak of excitation wavelength around 542.8 nm and emission at 565 nm. The
486 substrate, a 24 mm × 60 mm × 0.13 mm glass slide, is coated with a 20 µL droplet of 14 µM of
487 Rhodamine B in ethanol, which once evaporated provides a thin fluorescent layer which marks
488 the solid/air interface. The liquid marbles (50 µL) are made with a 10 µM Rhodamine B/water
489 solution, a concentration at which surface tension remains close to that of water [41]. Due to its
490 amphiphilic nature, Rhodamine B tends to adsorb at the liquid/air interface which reveals its
491 position. The fluorescent marbles are placed on the coated substrate (SI Appendix, Fig. S7a) and
492 the 3D structure of the air layer is obtained by taking 2D images at 200 different vertical positions
493 spaced by 1 to 4 µm using 552 nm excitation wavelength. The intensity I of the light emitted by
494 the Rhodamine B is averaged for each vertical position, it shows a first peak corresponding to the
495 substrate and a second one for the air/liquid interface of intensity I_o, which we use to normalize
496 the intensity. The air layer thickness H is defined as the distance between the substrate and the
497 bottom of the air-liquid interface given by $I/I_o = 0.18$ (SI Appendix, Fig. S7b).

498 **Glycerol vapor diffusion coefficient.** The diffusion coefficient of glycerol vapor is estimated by
499 the Chapman-Enskog kinetic theory in the rigid spheres approximation [39]:
500 $D = (3/8)\,[(N_A/(2\pi)(1/M_g+1/M_{air})]^{1/2} kT^{3/2}/(P_o\sigma_{AB}{}^2)$, with N_A the Avogadro number, M_g and M_{air} the
501 molar mass of glycerol and air, respectively, k the Boltzmann constant, P_o the atmospheric
502 pressure, and σ_{AB} is approximated to the diameter of glycerol molecules d = 5.47 Å. This gives a
503 typical value at room temperature of $D \approx 9.3$ mm^2 s^{-1}.

504

Acknowledgments

We thank David Quéré and Syuji Fujii for fruitful discussions. We thank Kazumasa Takeuchi for kindly allowing us to use his confocal microscope. We thank Kanata Hashimoto for the lycopodium photograph. TM and MT acknowledge the financial support provided by the Japan Society for the Promotion of Science (JSPS) - Grant-in-Aid for Scientific Research (B), 24K01341. TM and PKR gratefully acknowledge the financial support provided by the JSPS Grant-in-Aid for JSPS Fellows 23KF0106. MT appreciates support from WPI-MANA. YT is grateful for the financial support from JST SPRING (Grant Number JPMJSP2108) and the Leadership Development Program for Ph.D. students at the University of Tokyo, School of Engineering.

References

1. E. B. V. Dussan, R. T. P. Chow, On the ability of drops or bubbles to stick to non-horizontal surfaces of solids. *J. Fluid Mech.*, *137*, 1–29, (1983).

2. P. G. de Gennes, Wetting: Statics and dynamics. *Rev. Mod. Phys.*, *57*, 827–863, (1985).

3. C. Huh, L. E. Scriven, Hydrodynamic model of steady movement of a solid/liquid/fluid contact line. *J. Colloid Interface Sci.*, *35*, 85–101, (1971).

4. J. H. Snoeijer, B. Andreotti, Moving contact lines: Scales, regimes, and dynamical transitions. *Annu. Rev. Fluid Mech.*, *45*, 269–292, (2013).

5. R. Blossey, Self-cleaning surfaces – virtual realities. *Nat. Mater.*, *2,* 301–306, (2003).

6. A. Lafuma, D. Quéré, Superhydrophobic states. *Nat. Mater.*, *2*, 457–460, (2003).

7. P. Aussillous, D. Quéré, Liquid marbles. *Nature*, *411*, 924–927, (2001).

8. P. Jin, K. Zhao, Z. Blin, M. Allais, T. Mouterde, D. Quéré, When marbles challenge pearls. *J. Chem. Phys.*, *158*, 204709, (2023).

9. D. Quéré, The Mobility of Drops, Pearls, and Marbles. *Annual Review of Condensed Matter Physics*, *15*, 291-304 (2023).

10. C. Planchette, A. L. Biance, E. Lorenceau, Transition of liquid marble impacts onto solid surfaces. *Europhysics letters*, *97*, 14003, (2012).

11. M. Tenjimbayashi, S. Fujii, How liquid marbles break down: direct evidence for two breakage scenarios. *Small*, *17*, 2102438, (2021).

12. P. Papadopoulos, L. Mammen, X. Deng, D. Vollmer, and H. J. Butt, How superhydrophobicity breaks down. *Proceedings of the National Academy of Sciences*, *110*, 3254-3258, (2013).

13. M. Reyssat, A. Pépin, F. Marty, Y. Chen, D. Quéré, Bouncing transitions on microtextured materials. *Europhysics Letters*, *74*, 306-312, (2006).

14. D. Bartolo, F. Bouamrirene, E. Verneuil, A. Buguin, P. Silberzan, S. Moulinet, Bouncing or sticky droplets: Impalement transitions on superhydrophobic micropatterned surfaces. *Europhysics Letters*, *74*, 299-305, (2006).

15. G. McHale, M. I. Newton, Liquid marbles: Principles and applications. *Soft Matter*, *7*, 5473–5481, (2011).

16. E. Bormashenko, New insights into liquid marbles. *Soft Matter*, *8*, 11018–11021, (2012).

17. M. Tenjimbayashi, T. Mouterde, P.K. Roy, and K. Uto, Liquid Marble: Review of Recent Progress in Physical Properties, Formation Techniques, and Lab-in-a-Marble Applications in Microreactors and Biosensors. *Nanoscale*, *15*, 18980–18998, (2023).

18. Y. Zhao, J. Fang, H. Wang, X. Wang, and T. Lin, Magnetic liquid marbles: manipulation of liquid droplets using highly hydrophobic Fe3O4 nanoparticles. *Advanced materials*, *22*, 707-710, (2010).

19. C. S. L. Koh, H. K. Lee, G. C. Phan-Quang, X. Han, M. R. Lee, Z. Yang, and X. Y. Ling, SERS-and Electrochemically Active 3D Plasmonic Liquid Marbles for Molecular-Level Spectroelectrochemical Investigation of Microliter Reactions. *Angewandte Chemie*, *129*, 8939-8943, (2017).

20. N. M. Oliveira, R. L. Reis, and J. F. Mano, The potential of liquid marbles for biomedical applications: a critical review. Adv. Healthc. Mater., *6*, 1700192, (2017).

21. F. Sarvi, K. Jain, T. Arbatan, P. J. Verma, K. Hourigan, M. C. Thompson, W. Shen, and P. P. Y. Chan, Cardiogenesis of embryonic stem cells with liquid marble micro-bioreactor. Adv. Healthc. Mater., *4*, 77-86, (2015).

22. R. K. Vadivelu, H. Kamble, A. Munaz, and N. T. Nguyen, Liquid marble as bioreactor for engineering three-dimensional toroid tissues. *Scientific reports*, *7*, 12388 (2017).

23. Y. Sheng, G. Sun, J. Wu, G. Ma, and T. Ngai, Silica-based liquid marbles as microreactors for the silver mirror reaction. *Angewandte Chemie*, *127*, 7118-7123, (2015).

24. J. Tian, T. Arbatan, X. Li, and W. Shen, Liquid marble for gas sensing. *Chemical Communications*, *46*, 4734-4736, (2010).

25. S. Fujii, S. Kameyama, S. P. Armes, D. Dupin, M. Suzaki, and Y. Nakamura, pH-responsive liquid marbles stabilized with poly (2-vinylpyridine) particles. *Soft Matter*, *6*, 635-640, (2010).

26. X. Rong, R. Ettelaie, S. V. Lishchuk, H. Cheng, N. Zhao, F. Xiao, F. Cheng, and H. Yang, Liquid marble-derived solid-liquid hybrid superparticles for CO_2 capture. *Nat Commun*, *10*, 1854, (2019).

27. M. Paven, H. Mayama, T. Sekido, H-J. Butt, Y. Nakamura, and S. Fujii, Light-driven delivery and release of materials using liquid marbles. *Advanced Functional Materials*, *26*, 3199-3206. (2016).

28. M. Paven, “Fabrication and manipulation of non-wetting surfaces and drops: From super liquid- repellency and the Leidenfrost effect to liquid marbles,” Thesis, Johannes Gutenberg-Universität Mainz, (2016).

29. N. Kavokine, M. Anyfantakis, M. Morel, S. Rudiuk, T. Bickel, and D. Baigl, Light-driven transport of a liquid marble with and against surface flows. *Angewandte Chemie International Edition*, *55*, 11183-11187. (2016).

30. M. Uda, H. Kawashima, H. Mayama, T. Hirai, Y. Nakamura, and S. Fujii, Locomotion of a nonaqueous liquid marble induced by near-infrared-light irradiation. *Langmuir*, *37*, 4172-4182. (2021).

31. Z. Xu, Y. Zhao, L. Dai, and T. Lin, Multi-responsive janus liquid marbles: the effect of temperature and acidic/basic vapors. *Particle & Particle Systems Characterization*, *31*, 839-842. (2014).

32. C. Aberle, M. Lewis, G. Yu, N. Lei, and J. Xu, Liquid marbles as thermally robust droplets: coating-assisted Leidenfrost-like effect. *Soft Matter*, *7*, 11314-11318. (2011).

33. A. Hashmi, A. Strauss, and J. Xu, Freezing of a liquid marble. *Langmuir*, *28*, 10324-10328. (2012).

34. D. Zang, K. Lin, W. Wang, Y. Gu, Y. Zhang, X. Geng, and B. P. Binks, Tunable shape transformation of freezing liquid water marbles. *Soft Matter*, 10, 1309-1314. (2014).

35. K. R. Sreejith, P. Singha, N. K. Nguyen, C. H. Ooi, D. V. Dao, and N. T. Nguyen, Noninvasive refilling of liquid marbles with water for microfluidic applications. *Applied Physics Letters*, *120*. (2022).

36. P. Aussillous, and D. Quéré, Properties of liquid marbles, *Proc. R. Soc. A, 461*, 973-999, (2006).

37. D. Kane, and M. S. El-Shall, Condensation of supersaturated vapors of hydrogen bonding molecules: Ethylene glycol, propylene glycol, trimethylene glycol, and glycerol. The Journal of Chemical Physics, *105*, 7617, (1996).

38. S. P. Verevkin, D. H. Zaitsau, V. N. Emeléyanenko, and A. A. Zhabina, Thermodynamic properties of glycerol: Experimental and theoretical study. *Fluid Phase Equilibria*, *397*, 87-94, (2015).

39. R. B. Bird, W. E. Stewart, and E. N. Lightfoot, Transport Phenomena. 2nd edn. Wiley (2006).

40. T. Mouterde, G. Lehoucq, S. Xavier, A. Checco, C. T. Black, A. Rahman, T. Midavaine. C. Clanet, D. Quéré, Antifogging abilities of model nanotextures. *Nat. Mater.*, *16*, 658-663, (2017).

41. A. D. Smith McWilliams, S. Ergülen, M. M. Ogle, C. A. de los Reyes, M. Pasquali, and A. A. Marti, Fluorescent surfactants from common dyes – Rhodamine B and Eosin Y, *Pure Appl. Chem.* 92, 265–274, (2020).

Figure Legends.

Figure 1. Hot liquid marbles stability. **a,** Schematic of the experiment: a liquid marble of volume $\Omega = 50$ µL and temperature $T_o + \Delta T$ is placed on a silicon wafer kept at T_o. Inset: optical microscope image of the lycopodium grains of diameter 30 µm coating the liquid. **b,** Images of hot liquid marbles 3 minutes after being placed on the hydrophilic substrate (top) and hydrophobic substrate (bottom), for $\Delta T = 0$°C (left) and $\Delta T = 16$°C (right). **c,** Final apparent contact angle θ_f of liquid marbles placed on hydrophilic (blue data) or hydrophobic (red data) substrates as a function of the temperature difference ΔT. Plain lines are guides for the eyes. **d,** Time evolution of hot liquid marbles' apparent contact angle when placed on hydrophilic substrates for different ΔT. The vertical dashed lines mark the rupture time t_r. **e,** Rupture time of hot liquid marble placed on hydrophilic substrates as a function ΔT (red data). The black line represents Eq. (1) with $d \approx 19.7 \pm 2.1$ µm, the blue shaded area corresponding to the 95% interval of confidence. The red line represents the first-order Taylor expansion approximation ($d \approx 18.3 \pm 2.6$ µm) of Eq. (1) and the green area corresponds to the stable marble regime ($t_r > \tau$; $\Delta T < \Delta T_c$).

Figure 2. Condensation-induced rupture mechanism of hot liquid marbles on hydrophilic substrates. **a,** Schematic of the Total Internal Reflection setup. The hot liquid marble is placed on a glass substrate and the illumination incidence angle is between the total internal reflection angle for the glass/air and glass/water interfaces. When water contacts the interface, the light goes through the substrate and appears black on the high-speed camera image. **b,** TIR images below a liquid marble placed on a hydrophilic glass substrate in the isothermal case ($\Delta T = 0$°C). **c,** High-speed TIR images revealing the condensation process below a hot liquid marble ($\Delta T = 1.6$°C and $\Delta T = 16$°C) deposited on a hydrophilic glass substrate. The liquid marble ruptures from $t \approx 0.46$ s and rapidly spreads on the surface. **d,** Schematic of the air layer below the liquid marble showing the average air layer thickness H (top), and the condensation process at the minimum of the air layer thickness h. **e,** Evolution of the temperature difference ΔT as a function of time for different initial ΔT. The temperature is well fitted by an exponential decay $\Delta T(t = 0) = \Delta T_o \exp(-t/\tau)$ with a characteristic cooling time $\tau = 11$ s (plain lines).

Figure 3. Static friction of hot liquid marbles on hydrophobic substrates. **a,** Images of 50 µL lycopodium hot liquid marbles deposited on a hydrophobic surface just before rolling due to slope (left images), along with corresponding TIR images (right images), for ΔT = 3°C, 7°C and ΔT = 25°C from left to right. **b,** Evolution of the static friction force (red disks, left vertical axis) and the fraction of wetted area ϕ (blue triangles, right vertical axis) as a function of ΔT. **c,** Temperature-induced static friction $\Delta F = F - F(\Delta T = 0)$ plotted as a function of the fraction of wetted area ϕ. The red line represents the best linear fit obtained by multiplying Eq. (3) by a prefactor 1.19 ± 0.12, the 95% confidence interval is represented by the blue shaded area ($R^2 \approx 0.96$). **d,** log-log plot of the static friction of lycopodium hot liquid marbles as a function of their volume Ω for different ΔT. For small ΔT (blue data) the static friction varies linearly with the marble volume as described by the dry friction model of Eq. (2) plotted with a blue line. For larger ΔT, the friction nature changes to a wet static friction which increases with $\Omega^{1/2}$ as captured by our model, Eq. (3), which is plotted as a red line with a prefactor of 1.19.

Figure 4. Static friction of hot liquid marbles on hydrophobic substrates. **a,** Confocal images of the air layer of average height H between a glass substrate coated with dried Rhodamine B and liquid marbles filled with an aqueous solution of Rhodamine B and made with three kinds of particles: lycopodium, fumed silica nanoparticles and glass beads. **b,** Variation of static friction with ΔT for marbles made with fumed silica (H = 30 ± 3 µm, blue triangles), lycopodium (H = 56 ± 2 µm, red disks), and glass beads (H = 242 ± 8 µm, green squares). **c,** TIR images of water hot liquid marbles with ΔT = 29°C for: fumed silica (blue), lycopodium (red), and glass beads (green) and hot glycerol made with lycopodium (black). **d,** Evolution of the static friction as a function of ΔT for water (red disks) and glycerol (black diamonds) showing the effect of the liquid volatility on static friction. **e,** Plot of the ratio between the average air layer thickness H and the predicted maximum condensation height δ (Eq. 4) as a function of ΔT. We mark in green (resp. red) the low (resp. high) friction marbles defined by $\Delta F < F_{max}/2 = F_{wet}(\phi = 1)/2$ (resp. $\Delta F > F_{max}/2$). Our model predicts the friction transition to occur for $H/\delta \sim 1$ which is in excellent agreement with the line separating the two regimes $H/\delta \approx 0.35$.

Figure 5. Static friction of hot liquid marbles on nanostructured superhydrophobic substrates. **a,** Static friction of 50 µL lycopodium liquid marbles plotted as a function of the temperature difference for hydrophobic (red disks) and superhydrophobic (green triangles) substrates. **b,** Temperature-induced static friction $\Delta F = F - F(\Delta T = 0)$ normalized by $(1 + \cos \theta_o)$ plotted as a function of ΔT for the hydrophobic and superhydrophobic substrates.

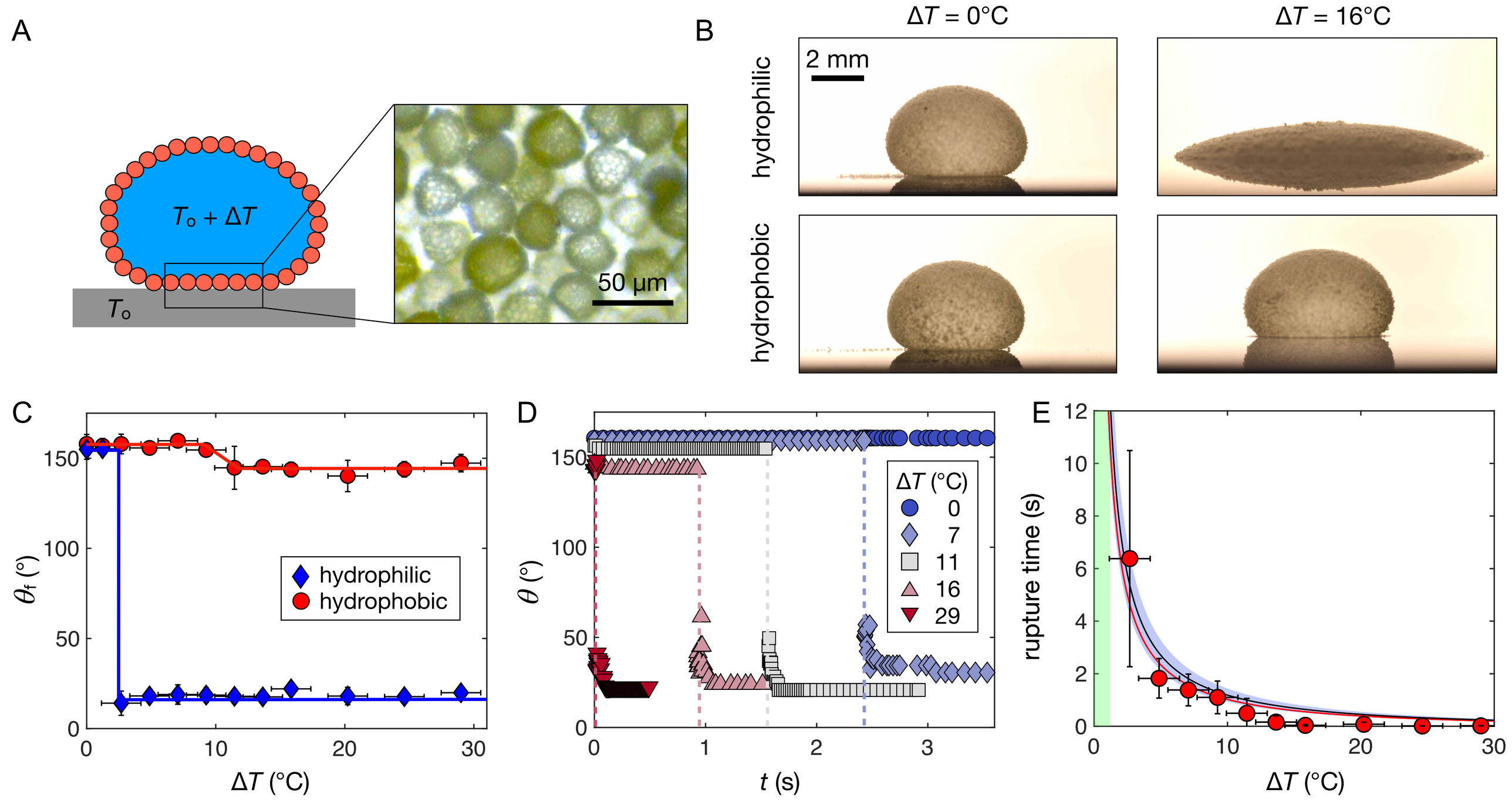
A
$T_o + \Delta T$
T_o
50 μm
B
ΔT = 0°C
ΔT = 16°C
hydrophilic
hydrophobic
2 mm
C
θ_f (°)
ΔT (°C)
hydrophilic
hydrophobic
D
θ (°)
t (s)
ΔT (°C)
0
7
11
16
29
E
rupture time (s)
ΔT (°C)

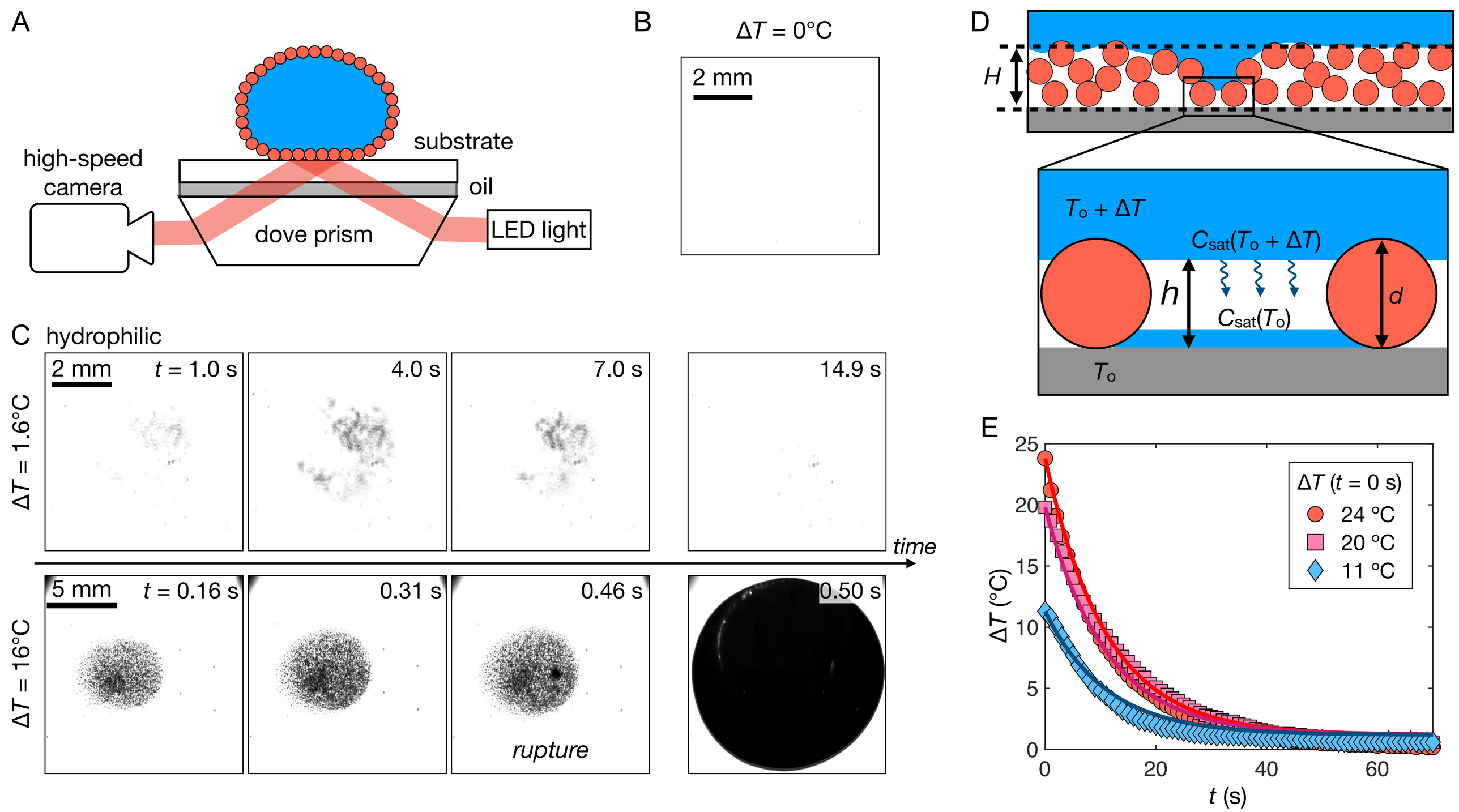
A
high-speed camera
substrate
oil
dove prism
LED light
B
ΔT = 0°C
2 mm
D
H
T_o + ΔT
C_sat(T_o + ΔT)
h
C_sat(T_o)
d
T_o
C
hydrophilic
ΔT = 1.6°C
2 mm
t = 1.0 s
4.0 s
7.0 s
14.9 s
time
ΔT = 16°C
5 mm
t = 0.16 s
0.31 s
0.46 s
rupture
0.50 s
E
ΔT (t = 0 s)
24 °C
20 °C
11 °C
ΔT (°C)
t (s)

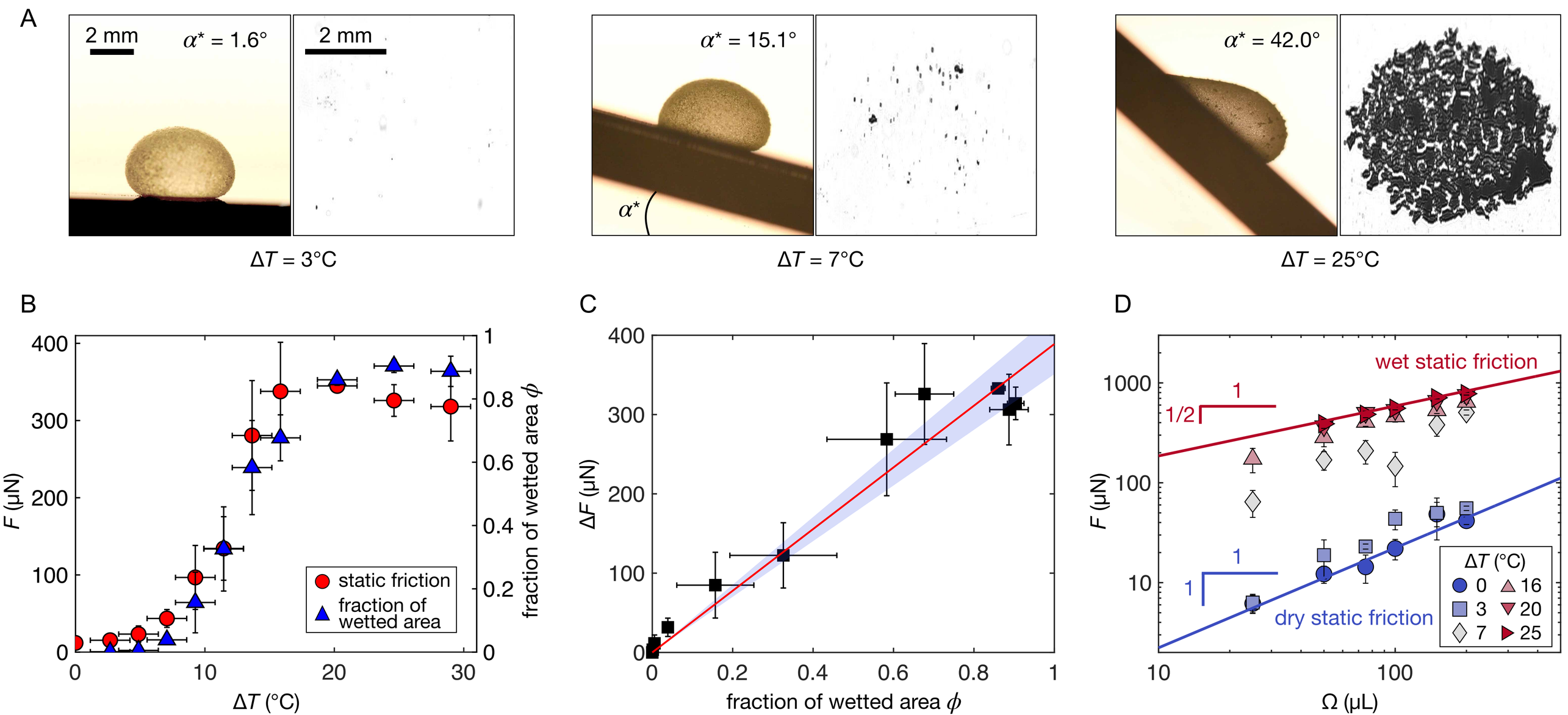
A
2 mm
α* = 1.6°
2 mm
α* = 15.1°
α*
α* = 42.0°
ΔT = 3°C
ΔT = 7°C
ΔT = 25°C
B
F (μN)
fraction of wetted area ϕ
ΔT (°C)
static friction
fraction of wetted area
C
ΔF (μN)
fraction of wetted area ϕ
D
F (μN)
Ω (μL)
wet static friction
dry static friction
1/2
1
1
1
ΔT (°C)
0
3
7
16
20
25

A

Air layer thickness

lycopodium

fumed silica

glass beads

100 µm

B

Effect of particle size

Ω = 50 µL

H (µm)
30
56
242

F (µN)

Δ*T* (°C)

C

Δ*T* = 29°C

30 µm | water

56 µm | water

242 µm | water

2 mm

56 µm | glycerol

D

Effect of liquid volatility

Ω = 50 µL

water
glycerol

F (µN)

Δ*T* (°C)

E

H (µm)
30
56
242
56 (gly)

low static friction

high static friction

H/δ

Δ*T* (°C)

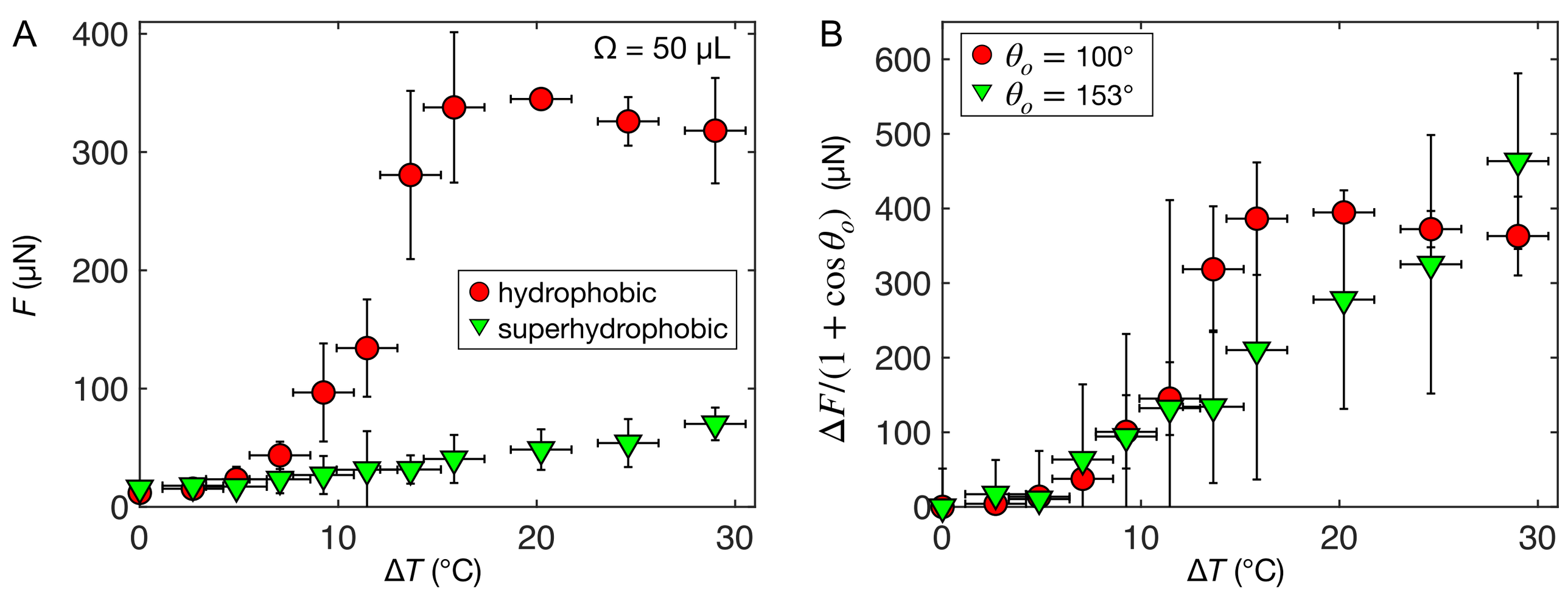
A
Ω = 50 μL
hydrophobic
superhydrophobic
F (μN)
ΔT (°C)
0
100
200
300
400
0
10
20
30
B
θ_o = 100°
θ_o = 153°
ΔF/(1 + cos θ_o) (μN)
ΔT (°C)
0
100
200
300
400
500
600
0
10
20
30